International Journal of
MATERIALS RESEARCH

Zeitschrift für METALLKUNDE

Original Contributions

Zhijun Ma[a], Zhong Yang[a], Yongchun Guo[a], Dong Tao[a], Jianping Li[a], Shaogang Wang[b]
[a] School of Materials and Chemical Engineering, Xi'an Technological University, Xi'an, P.R. China
[b] Institute of Metal Research, Chinese Academy of Sciences, Shenyang, P.R. China

3D morphology characterization of graphite and its effect on the thermal conductivity of vermicular graphite iron

It is important to establish the quantitative effect of graphite's 3D morphology on the thermal conductivity of vermicular graphite iron. In the present study, X-ray tomography is utilized to investigate the 3D morphology of graphite in vermicular graphite iron with different vermicularity. A 3D finite element model was built on the basis of graphite's 3D morphology and the equivalent thermal conductivity of vermicular graphite iron can be calculated. The results show that the volume of graphite clusters in vermicular graphite iron is distributed according to $y = a(1 - e^{-bx})^c$ exponential function. The higher the vermicularity, the more obvious the polarization of graphite volume. Compared with vermicularity, 3D connectivity of graphite is a more appropriate characteristic parameter to investigate the thermal conductivity of vermicular graphite iron from the 3D morphology point of view.

Keywords: Vermicular graphite iron; Thermal conductivity; 3D connectivity; X-ray tomography

1. Introduction

The unique mechanical and physical properties of vermicular graphite iron (VGI) have gained the material desirability and increasing demand in both automotive and locomotive industries, for example the cylinder heads of diesel engines. Especially for high power density diesel engines, whether from the viewpoint of the volume size, corrosion resistance and strength, or the friction coefficient of the engine, VGI is obviously better than aluminum alloy [1–5]. The increase of engine specific power brings about the working temperature rise of the cylinder head, and then the mechanical properties of VGI are also subject to higher requirements. However, with the decreasing of the latent capacity of mechanical properties, physical properties of cast iron, especially the thermal conductivity, have received more and more attention since the ability to transfer away heat enhances the resistance to such factors as thermal fatigue and distortion [6–10].

There are many factors affecting the thermal conductivity and interacting with each other. Most materials scientists think distribution and morphology of the graphite phase play the key role on thermal transport since thermal conductivity of graphite is significantly higher than that of the matrix in cast irons [10–14]. Some other factors also affect the thermal conductivity of cast iron, for example, pearlite content, alloy composition, carbon content, 3D connectivity of the graphite, and so on [15–17]. In current research and industrial production to evaluate the properties of cast iron relies mainly on the subjective comparison of 2D metallographic images. As the main characteristic of graphite's 3D morphology, although the complex 3D connectivity of the graphite network in flake graphite iron and VGI is believed to have an important effect on thermal conductivity [16, 17], the related research and development are not sufficient because its acquisition and quantitative characterization are difficult, for example the traditional deep etching method [18] or the serial sectioning method [19].

Some progress has been made in recent years to address these issues [20–28], such as the 3D characterization of graphite morphology by destructive focused ion beam (FIB) tomography [22–24] and X-ray tomography (XRT) [26–28]. Pina et al. [16] used an idealized unit cell model to represent the complex 3D microstructure of lamellar cast iron and quantitatively analyzed the thermal, mechanical and thermo-mechanical response of the unit cell by means of the finite element (FE) method. However, the relationship between 3D connectivity of the graphite phase and thermal conductivity of cast iron is still only at the qualitative stage.

In the present study, XRT is utilized to investigate 3D morphology and connectivity of graphite in VGI with different vermicularity which was sand cast by the authors Yang et al. [29, 30]. The probability distribution function of graphite particle volume was then built to quantitatively analyze the 3D morphology of graphite in VGI according to XRT statistics. In addition, a 3D FE model was built on the basis of graphite 3D morphology and the equivalent thermal conductivity of VGI could be calculated. The quantitative effect of graphite's connectivity on the thermal conductivity is attempted to be analyzed according to different FE model of VGI with different vermicularity. These stud-

Table 1. The nominal composition of the VGI samples.

Element	C	Si	Mn	S	P	Fe
wt.%	3.7–3.8	2.0–2.1	≤0.2	<0.06	<0.09	balance

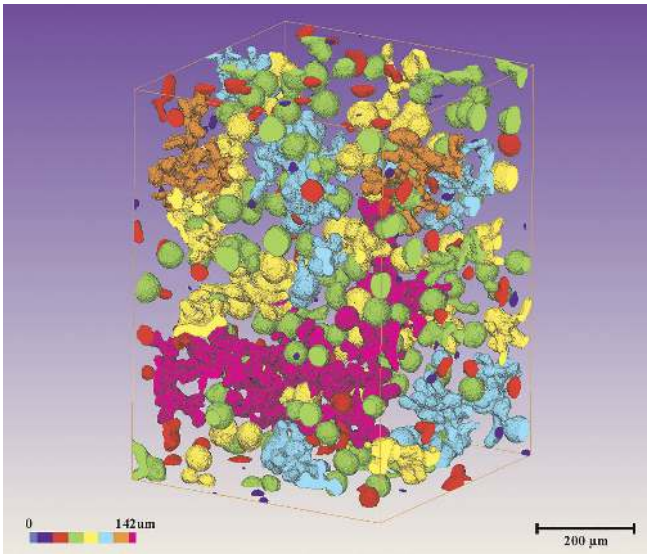

(a)

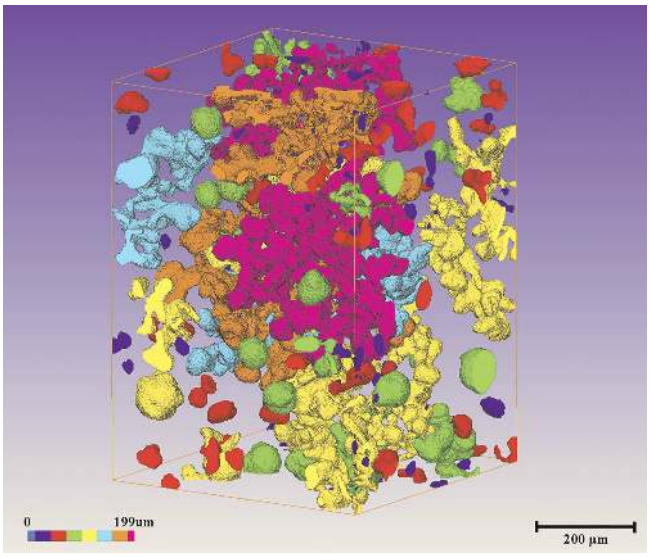

(b)

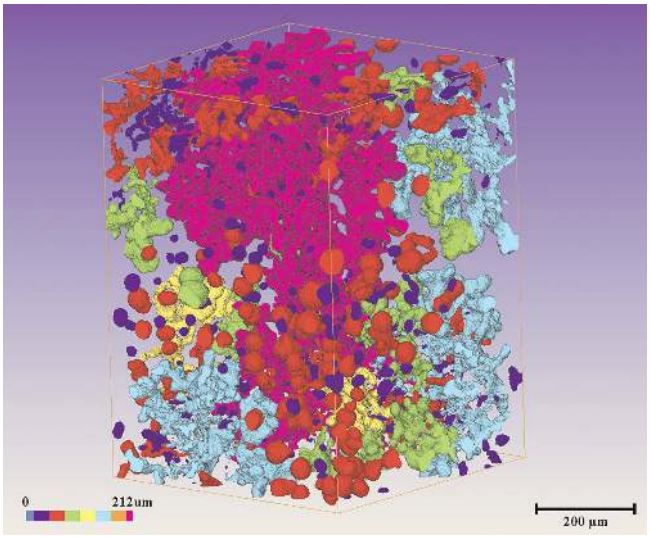

(c)

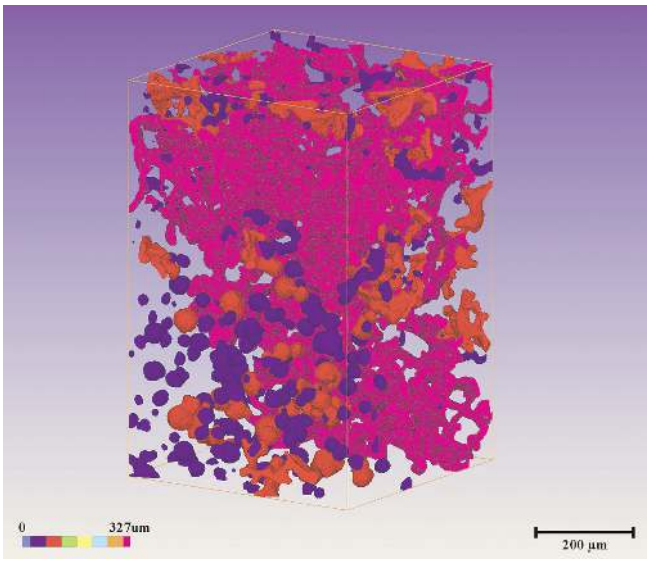

(d)

Fig. 1. The spatial structure and morphology of graphite in VGI with different vermicularity: (a) 60%; (b) 70%; (c) 80%; (d) 90%.

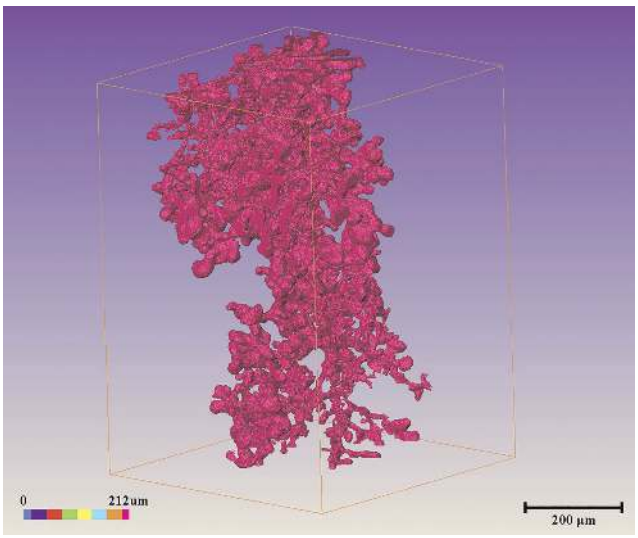

(a)

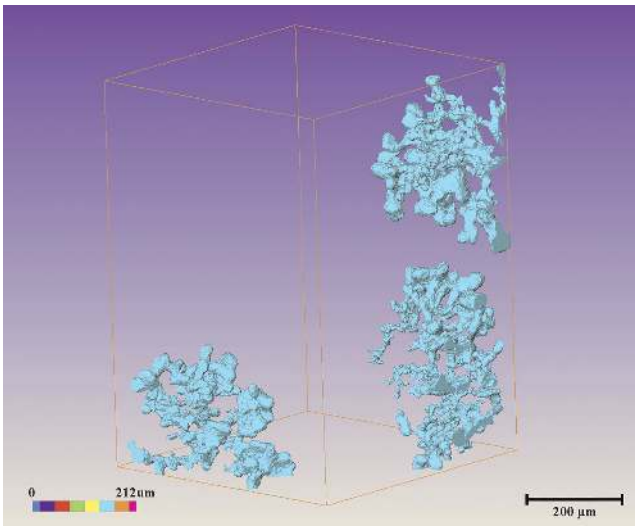

(b)

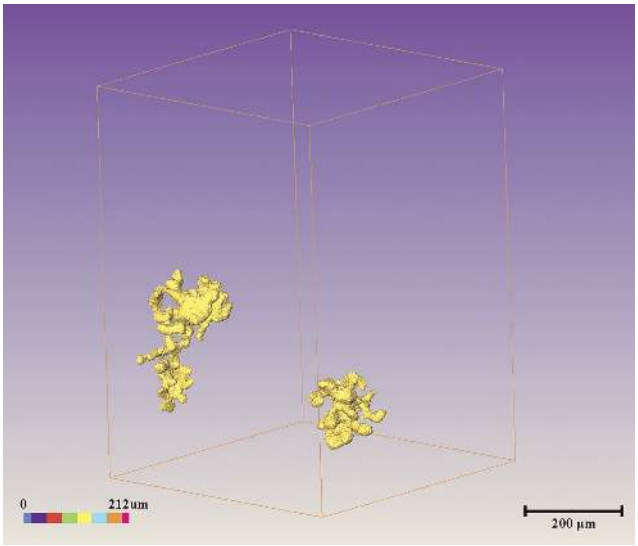

(c)

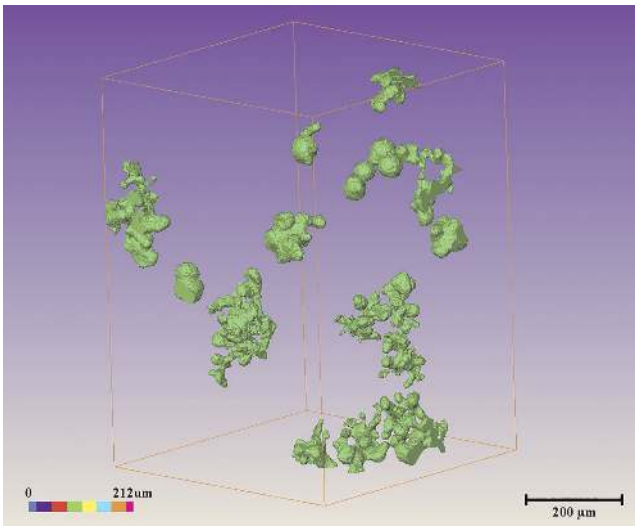

(d)

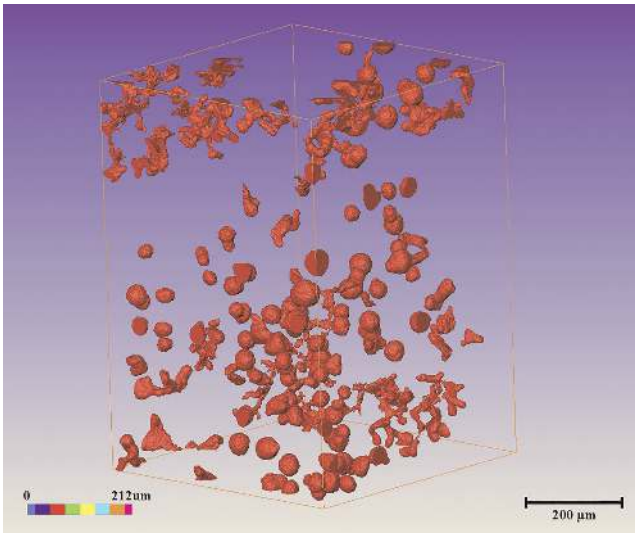

(e)

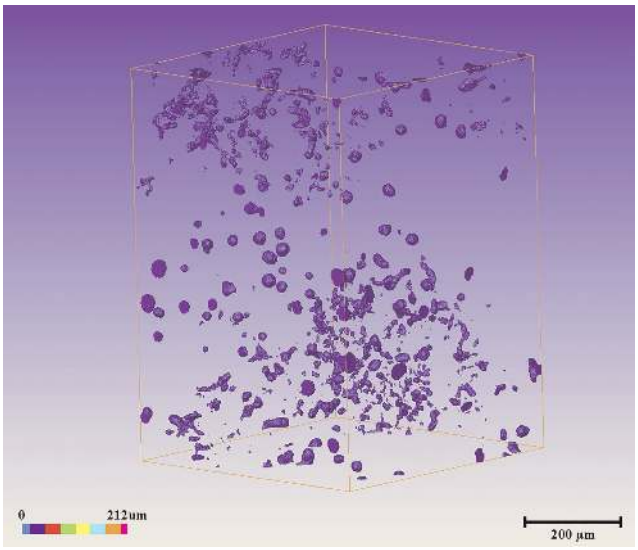

(f)

Fig. 2. Size grading display of graphite according to D_{equ} in VGI with 80 % vermicularity: (a) $D_{equ} > 200$ µm; (b) 145 µm > $D_{equ} > 200$µm; (c) 100 µm > $D_{equ} > 145$ µm; (d) 55 µm > $D_{equ} > 100$ µm; (d) 10 µm > $D_{equ} > 55$ µm; (d) 10 µm > D_{equ}.

ies can make it possible to predict thermal conductivity changes of VGI with relatively high accuracy and provide some constructive suggestions to improve the thermal conductivity of cast iron.

2. Experimental procedure

The microstructure and properties of VGI lie between gray cast iron and nodular graphite cast iron. Its chemical composition is similar to nodular graphite cast iron. Table 1 shows the nominal composition of VGI samples used in this study. VGI samples with different vermicularity (60 %, 70 %, 80 % and 90 %) can be prepared by adjusting the quantity of vermicular agent. Because the distribution of graphite is not completely uniform, different sites of the same sample will get different vermicularity. The calculation method of vermicularity is as follows. At ten different locations of the same sample metallographic photographs, the percentage of vermicular graphite area to all graphite areas is counted. The final vermicularity is the proximal integer obtained by averaging these ten percentages. Finally, four specimens with different vermicularity were selected for analysis and research.

Compared with 2D morphology, 3D morphology can reveal the microstructural characteristics of materials more comprehensively. The 3D morphology of graphite phase in VGI was investigated using a Xradia Versa XRM-500 XRT and reconstructed by Avizo image processing software. The test sample's size was ø 1.5×5 mm and voxel size of the present experimental setup was $1.1981 \times 1.1981 \times 1.1981$ μm^3. A $450 \times 450 \times 700$ voxels unit cell was extracted from columnar sample to characterize the 3D morphology of graphite phase using Avizo software.

A $569 \times 534 \times 365$ voxels unit cell was also extracted to

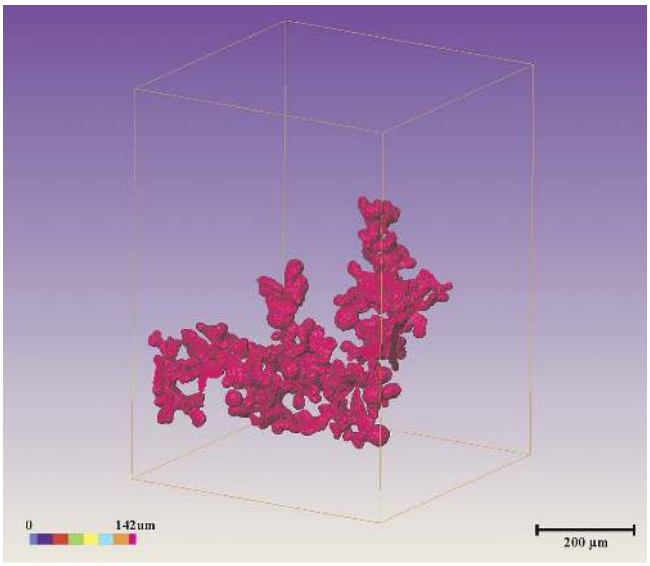

(a)

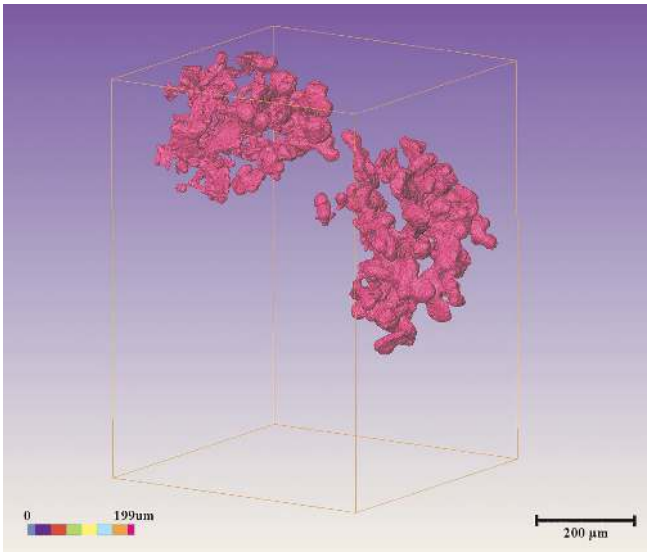

(b)

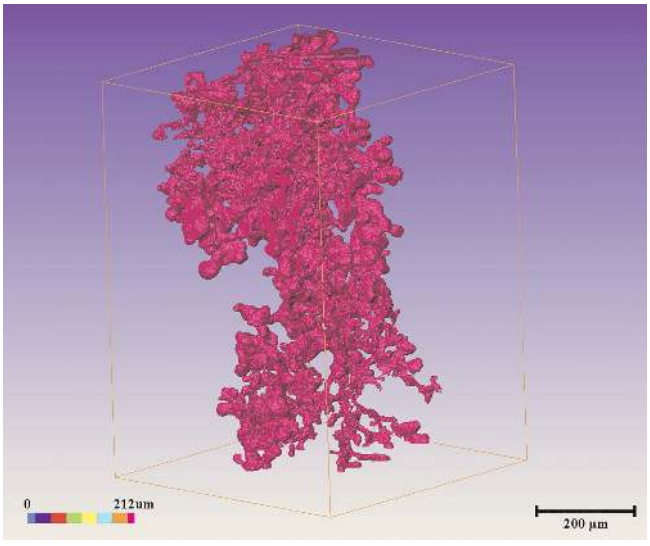

(c)

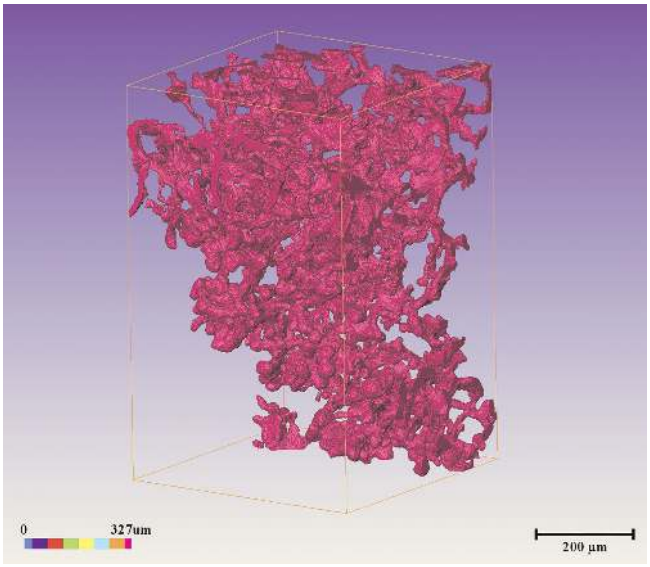

(d)

Fig. 3. The spatial structure and morphology of the largest graphite cluster in VGI with different vermicularity: (a) 60 %; (b) 70 %; (c) 80 %; (d) 90 %.

characterize the 3D morphology of graphite by the connectivity. The connectivity is defined in this work as the relative volume fraction of the largest particle of graphite with respect to the total volume fraction of graphite in the analyzed unit cell. A 3D FE model was then built in order to calculate the equivalent thermal conductivity of VGI. The quantitative relationship between 3D morphology of graphite and the thermal conductivity of VGI was tentatively established.

3. Results and discussion

3.1. 3D morphology characterization of graphite in VGI with different vermicularity

Figure 1 shows the spatial structure and morphology of graphite in VGI with different vermicularity (60 %, 70 %, 80 % and 90 % respectively). Different color rendering represents size grades of isolated graphite clusters. With the increase in vermicularity, the stubby graphite phase which is similar to nodular graphite cast iron turns into a fine network. In other words, the thickness of graphite is getting thinner and thinner. The cross-sectional morphology of VGI with 90 % vermicularity exhibits roughly flake graphite features. In the case of constant volume of graphite, the distribution of graphite phase is more and more uniform in VGI to some extent.

Take VGI with 80 % vermicularity as an example, size grading of graphite according to equivalent diameter D_{equ} is shown in Fig. 2. The D_{equ} of the largest graphite cluster is about 212 μm. There are only 7 graphite clusters over D_{equ} 100 μm and the number of the remaining graphite is about more than 1000. Most of the smaller graphite is spherical with different sizes. The large size graphite shows clear coral like microstructure and is almost all truncated by the boundary of the unit cell. In fact, the complete coral like graphite individual particles, the isolated graphite in the so-called eutectic grain formed during solidification process [31], have not been found in the size range ($\sim\varnothing$ 1.5 × 5 mm) of the test samples so far. This result is similar to the research of Chuang et al. [26] which points out that the entire picture of each individual CG (compacted graphite) is not revealed completely.

The 3D connectivity of graphite in VGI can be more clearly demonstrated if the largest graphite cluster is separately taken out to discuss in detail. The spatial structure and morphology of the largest graphite cluster in VGI with different vermicularity is shown in Fig. 3. The D_{equ} of the largest graphite cluster is 142 μm, 199 μm, 212 μm and 326 μm corresponding to 60 %, 70 %, 80 % and 90 % vermicularity respectively. With the increase in vermicularity, the dimension of the largest graphite cluster is getting bigger. Especially for 90 % vermicularity, the largest graphite cluster almost runs through the whole unit cell. The 3D connectivity of graphite in VGI is characterized by the ratio of the maximum graphite volume to the volume of all graphite in the corresponding vermicularity VGI. Then the higher

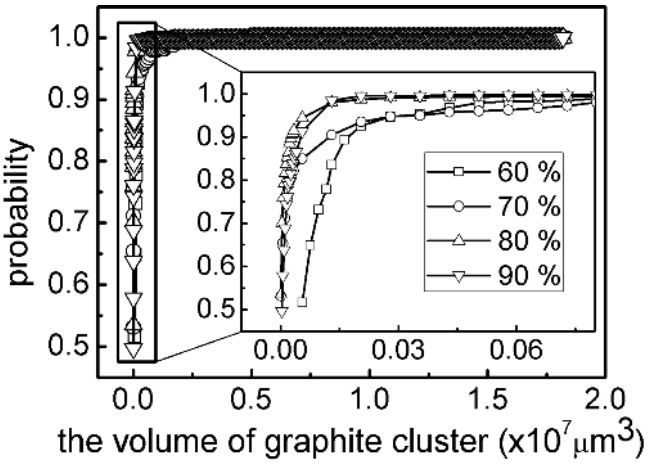

Fig. 4. The probability statistical distribution of graphite cluster volume in VGI with different vermicularity.

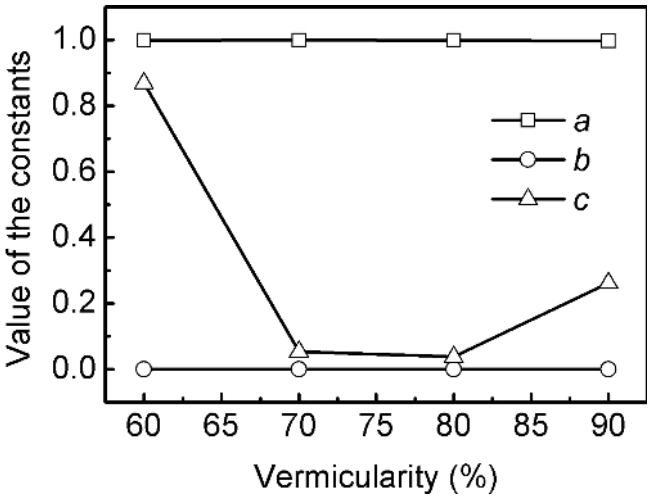

Fig. 5. Value of the constants in $y = a(1 - e^{-bx})^c$ exponential function with the change in vermicularity.

Table 2. The top ten graphite cluster's volume in different VGI samples (unit: $\times 10^7 \mu m^3$).

volume ($\times 10^7$ μm^3) / No. / Vermicularity	1	2	3	4	5	6	7	8	9	10
60 %	0.150	0.138	0.124	0.096	0.076	0.070	0.055	0.048	0.048	0.048
70 %	0.411	0.283	0.194	0.176	0.173	0.141	0.138	0.105	0.076	0.075
80 %	0.497	0.487	0.334	0.164	0.163	0.151	0.060	0.051	0.038	0.029
90 %	1.817	0.036	0.019	0.017	0.017	0.015	0.014	0.013	0.012	0.012

the vermicularity, the higher the 3D connectivity and the smaller the cross-sectional area of graphite.

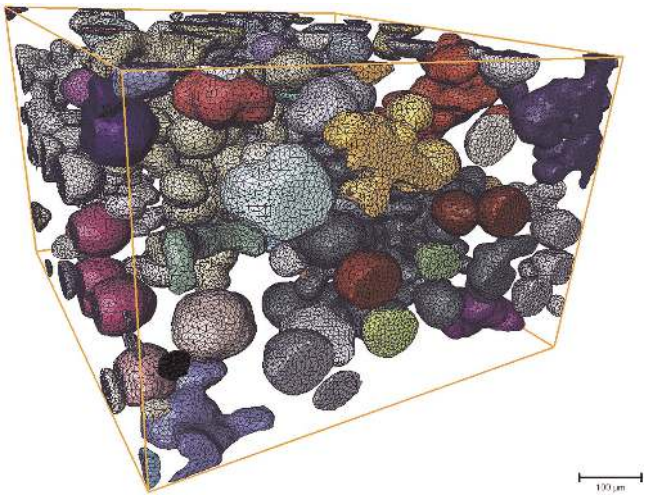

(a)

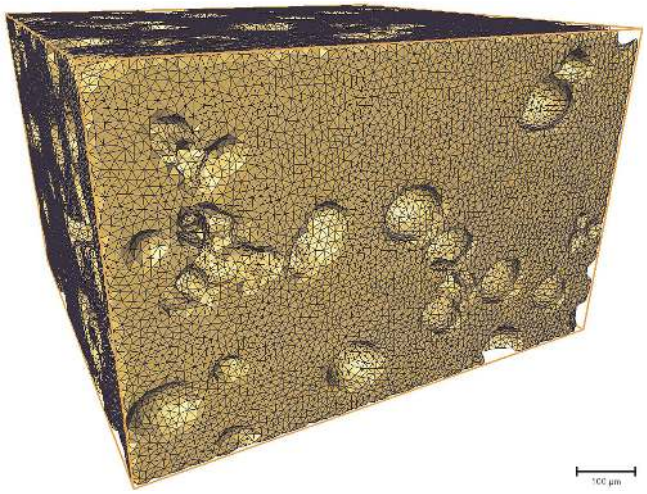

(b)

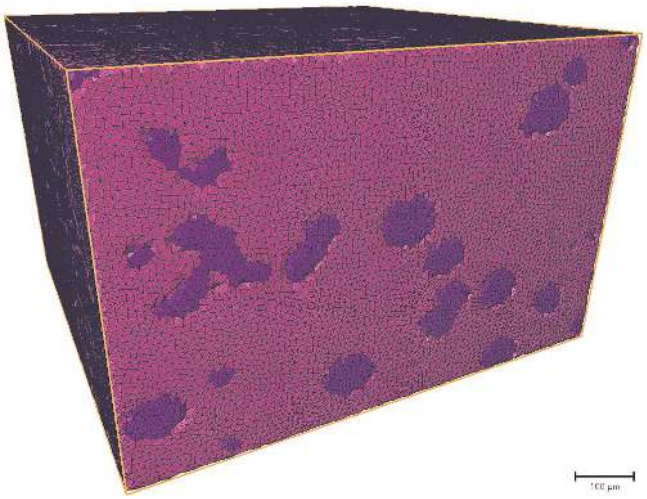

(c)

Fig. 6. The 3D FE mesh model of VGI with 60 % vermicularity: (a) graphite; (b) matrix; (c) VGI including graphite and matrix.

In order to further clarify the quantitative difference of graphite morphological character between different VGI samples, probability statistical distribution is also discussed according to graphite cluster volume, as shown in Fig. 4. The section marked by a box is magnified and shown in the inset so as to distinguish four curves clearly. In addition, the top ten graphite cluster volumes in different VGI samples is listed in Table 2. It can be seen that more than 95 % of graphite clusters are less than 3×10^5 μm^3 in volume as a whole. For 90 % vermicularity VGI, there are only two graphite clusters whose volume is more than 3×10^5 μm^3. Morever, the graphite volume in VGI is distributed according to $y = a(1 - e^{-bx})^c$ exponential function and Fig. 5 shows the values of the constants with the change in vermicularity. The values of a and b are basically fixed and close to 1 and 0 respectively. The value of c decreases from 0.8683 at 60 % vermicularity and then increases with the vermicularity, and the lowest value of c is at 80 % vermicularity. The graphite volume distribution of 60 % vermicularity VGI is obviously more uniform than that of 80 % and 90 % vermicularity VGI. The higher the vermicularity, the more the polarization of graphite volume.

3.2. The effect of 3D morphology of graphite on the thermal conductivity of VGI with different vermicularity

FE-simulations were carried out on the basis of 3D morphology of VGI (shown in Fig. 1). Suppose the FE physical model would only contain two phases, graphite and matrix. The corresponding thermal conductivity is 130 W m^{-1} K^{-1} [32] and 30 W m^{-1} K^{-1} respectively. The physical model can be meshed in Avizo software. Take VGI with 60 % vermicularity as an example, the corresponding 3D FE mesh model of graphite, matrix and VGI is shown in Fig. 6a, b and c, respectively. The Thermal Solid Tet 10 node 87 element is applied, and then the FE mesh of VGI is imported into ANSYS software to simulate a steady heat transfer process.

During the simulation process, fixed temperature and convective heat transfer boundary condition are defined on the two 534×365 voxels faces. The adiabatic boundary condition is set up on the other faces of the model. The distribution of temperature and heat flux at a steady heat transfer boundary condition can then be obtained from numerical simulation.

The equivalent isotropic thermal conductivity k_e can be derived according to Eq. (1) [33]. In Eq. (1), Φ is heat flow, A is area for heat conduction and dt/dx is temperature gradient, a_i is the area of the No.i element's plane perpendicular to the direction of heat transfer and q_i the corresponding heat flux. The objective of the following simulations is to evaluate the thermal conductivity of VGI through the distribution of temperature and heat flux.

$$k_e = -\frac{\Phi}{A} \Big/ \frac{dt}{dx} = -\frac{\sum_{i=1}^{m} q_i a_i}{\sum_{i=1}^{m} a_i} \Big/ \frac{dt}{dx} \tag{1}$$

Figure 7 shows the temperature and heat flux distribution of VGI with 60 % and 90 % vermicularity at a steady heat

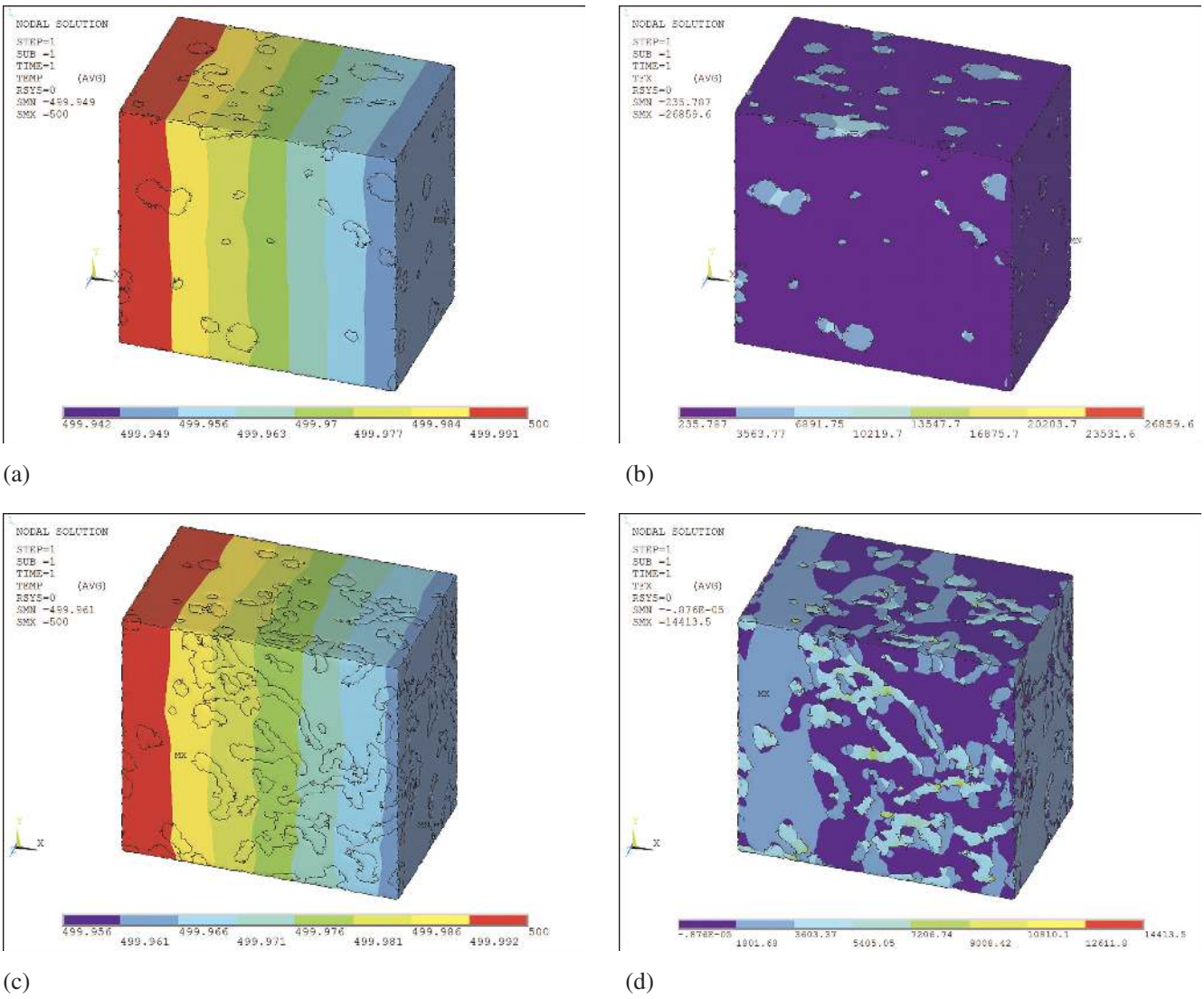

Fig. 7. The temperature and heat flux distribution of VGI with 60 % and 90 % vermicularity at a steady heat transfer boundary condition: (a) temperature distribution of VGI with 60 % vermicularity; (b) heat flux distribution of VGI with 60 % vermicularity; (c) temperature distribution of VGI with 90 % vermicularity; (d) heat flux distribution of VGI with 90 % vermicularity.

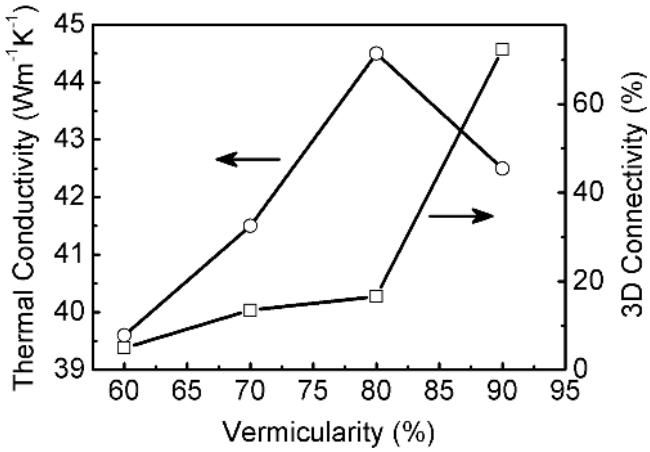

Fig. 8. The change in thermal conductivity and 3D connectivity with vermicularity.

transfer boundary condition. Generally the graphite phase has a great impact on the thermal conductivity of cast iron. There exist obvious non-even characteristics in the distribution of temperature and heat flux. Heat transfer is mainly carried out by graphite since the thermal conductivity of graphite is much higher than that of the matrix (Fig. 7b and d), whereas the average heat flux in VGI with 90 % vermicularity is slightly larger than that in VGI with 60 % vermicularity. This difference should be mainly due to the 3D morphology difference of graphite phase.

The equivalent thermal conductivity k_e of VGI with different vermicularity can be derived according to Eq. (1). The calculated thermal conductivity is a little higher than the experimental value in most literature [6, 9, 34]. Besides the inaccuracy of material properties, the influence of interface on the thermal conductivity is one of main reasons [35]. The change in thermal conductivity with vermicularity is shown in Fig. 8. The thermal conductivity of VGI increases with the increase in vermicularity. When the vermicularity is 80 %, the thermal conductivity reaches a maximum and then

decreases. Coincidentally, the value of c in the graphite volume distribution function $y = a(1 - e^{-bx})^c$ is the lowest when the vermicularity is 80 %. In addition, the relationship between the 3D connectivity and the vermicularity is also shown in Fig. 8. As can be seen from the diagram, the vermicularity and 3D connectivity are not completely linear, especially when the vermicularity is over 80 %, the connectivity of the vermicular graphite will rise sharply. In other words, there also exists an obvious inflection point in the change process of 3D connectivity with vermicularity. But its change trend is different from the thermal conductivity.

It can be seen from the above FE calculation results that too high vermicularity or 3D connectivity would decrease the thermal conductivity of VGI. Although high 3D connectivity of graphite can provide a more continuous heat transfer channel, the cross-sectional area of graphite is sharply reduced at the same content of graphite. This reduces the heat transfer efficiency of the graphite cluster. Therefore, there exists a peak value of the thermal conductivity at about 80 % vermicularity of VGI or 17 % 3D connectivity of graphite phase.

4. Conclusion

In the present study, XRT was utilized to investigate the 3D morphology and connectivity of graphite in VGI with different vermicularity. The probability distribution function of a graphite cluster's volume was then fitted to quantitatively analyze the 3D morphology of graphite in VGI according to XRT statistics. On the basis of the graphite's 3D morphology the equivalent thermal conductivity of VGI can be quantitatively calculated by means of FE methods. Some conclusions can be drawn as follows:

1. The graphite phase is stubby when the vermicularity is low, and changes into coral-like, and finally a fine network with the increase in vermicularity. The dimension of the largest graphite cluster in the unit cell increases. For 90 % vermicularity the largest graphite cluster almost runs through the whole unit cell.
2. The graphite volume in VGI is distributed according to $y = a(1\text{-}e^{-bx})^c$ exponential function. The higher the vermicularity, the more obvious the polarization of graphite volume.
3. The vermicularity and 3D connectivity are not completely linear, especially when the vermicularity is over 80 %, the connectivity of the vermicular graphite will rise sharply. There exists an obvious inflection point in the change process of 3D connectivity and thermal conductivity with vermicularity. The 3D connectivity of graphite can also be used to investigate the thermal conductivity of VGI from the 3D morphology point of view.

The authors would like to acknowledge the financial support of the Key Research Program of Shaanxi Provincial Department of Technology and Science (2018ZDXM-GY-137), the Serving Local Special Project of Shaanxi Provincial Department (18JC013) and Key Research and Development Plan of Shanxi Province Industrial Project (2018GY-111).

References

[1] S. Dawson: China Foundry. 6 (2009) 241. DOI:10.1016/S1006-7191(08)60104-0
[2] X.X. Zhang, G.W. Zhang, H. Xu: Hot Working Tech. 43 (2014) 27. DOI:10.14158/j.cnki.1001-3814.2014.13.053
[3] X.X. Wang, J.R. Zhou, W. Su: J. Netshape Forming Eng. 2 (2010) 79. DOI:10.3969/j.issn.1674-6457.2010.06.020
[4] M. Li: Internal Combustion Engine & Powerplant 4 (2010) 49. DOI:10.3969/j.issn.1673-6397.2010.04.014
[5] V. Norman, P. Skoglund, D. Leidermark, J. Moverare: Int. J. Fatigue. 80 (2015) 381. DOI:10.1016/j.ijfatigue.2015.06.005
[6] D. Holmgren: Int. J. Cast Met. Res. 18 (2005) 331. DOI:10.1179/136404605225023153
[7] D. Holmgren, A. Dioszegi, I.L. Svensson: Int. J. Cast Met. Res. 20 (2007) 30. DOI:10.1179/136404607X202690
[8] D. Holmgren, R. Kallbom, I.L. Svensson: Metall. Mater. Trans. A. 38 (2007) 268. DOI:10.1007/s11661-006-9016-2
[9] M. Selin, D. Holmgren, I.L. Svensson: Int. J. Cast Met. Res. 22 (2009) 283. DOI:10.1179/136404609x367984
[10] A. Velichko, A. Wiegmann, F. Mücklich: Acta Mater. 57 (2009) 5023. DOI:10.1016/j.actamat.2009.07.004
[11] R.L. Hecht, R.B. Dinwiddie, H. Wang: J. Mater. Sci. 34 (1999) 4775. DOI:10.1023/A:1004643322951
[12] X.X. Zhang, L.J. Liu: China Foundry Mach. Tech. 2 (2012) 6. DOI:10.3969/j.issn.1006-9658.2012.02.002
[13] A. Velichko, F. Mücklich: Prakt. Metallogr. 43 (2006) 192. DOI:10.22028/D291-22318
[14] J. Helsing, G. Grimvall: J. Appl. Phys. 70 (1991) 1198. DOI:10.1063/1.349573
[15] G.W. Guo, H.X. Ma, J. Zhang: Phys. Testing Chem. Anal. Part A (Phys. Anal.) 41 (2005) 13. DOI:10.3969/j.issn.1001-4012.2005.01.003
[16] J.C. Pina, V.G. Kouznetsova, M.G.D. Geers: Int. J. Solids Struct. 63 (2015) 153 – 166. DOI:10.1016/j.ijsolstr.2015.02.048
[17] J.C. Pina, S. Shafqat, V.G. Kouznetsova, J.P.M. Hoefnagels, M.G.D. Geers: Mater. Sci. Eng. A 658 (2016) 439. DOI:10.1016/j.msea.2016.02.017
[18] A. Velichko, C. Holzapfel, A. Siefers, K. Schladitz, F. Mücklich: Acta Mater. 56 (2008) 1981. DOI:10.1016/j.actamat.2007.12.033
[19] M. Metzger, T. Seifert: Int. J. Solids Struct. 66 (2015) 184. DOI:10.1016/j.ijsolstr.2015.04.014
[20] G. Fischer, J. Nellesen, N.B. Anar, K. Ehrig, H. Riesemeier, W. Tillmann: Mater. Sci. Eng. A 577 (2013) 202. DOI:10.1016/j.msea.2013.04.057
[21] J.M. Li, L. Lu, M.O. Lai: Mater. Charact. 45 (2000) 83. DOI:10.1016/s1044-5803(00)00052-8
[22] A. Velichko, C. Holzapfel, F. Mücklich: Adv. Eng. Mater. 9 (2007) 39. DOI:10.1002/adem.200790000
[23] A. Hatton, M. Engstler, P. Leibenguth, F. Mücklich: Adv. Eng. Mater. 13 (2011) 136. DOI:10.1002/adem.201000234
[24] A. Velichko, F. Mücklich: Int. J. Mater. Res. 100 (2009) 1031. DOI:10.3139/146.110148
[25] V.D. Cocco, D. Iacoviello, F. Iacoviello, A. Rossi: Procedia Eng. 109 (2015) 135. DOI:10.1016/j.proeng.2015.06.223
[26] C. Chuang, D. Singh, P. Kenesei, J. Almer, J. Hryn, R. Huff: Scr. Mate. 106 (2015) 5. DOI:10.1016/j.scriptamat.2015.03.017
[27] S.R. Stock: Int. Mater. Rev. 44 (1999) 141. DOI:10.1179/095066099101528261
[28] Y.Z. Liu, Y.F. Li, J.D. Xing, S.G. Wang, B.C. Zheng, D. Tao, W. Li: Mater. Charact. 144 (2018) 155. DOI:10.1016/j.matchar.2018.07.001
[29] Z. Yang, X.G. Yang, Y.H. Zhao, T. Yang, J.P. Li, D. Tao: Foundry Tech. 36 (2015) 1518. DOI:10.16410/j.issn1000-8365.2015.06.056
[30] Z. Yang, D. Tao, Y.C. Guo, T. Yang, J.P. Li: Foundry, 63 (2014) 115. DOI:10.3969/j.issn.1001-4977.2014.02.003
[31] D.M. Stefanescu, G. Alonso, P. Larrañaga, R. Suarez: Acta Mater. 103 (2016) 103. DOI:10.1016/j.actamat.2015.09.043
[32] G. Ljustina, R. Larsson, M. Fagerström: Finite Elem. Anal. Des. 80 (2014) 1. DOI:10.1016/j.finel.2013.10.006
[33] S.D. Lu, X.G. Gao, Y.D. Song: J. Aero. Power 29 (2014) 1574. DOI:10.13224/j.cnki.jasp.2014.07.009

[34] Y.Z. Liu, Y.F. Li, J.D. Xing, S.G. Wang, B.C. Zheng, D. Tao, W. Li: Mater. Charact. 144 (2018) 155. DOI:10.1016/j.matchar.2018.07.001
[35] Z.J. Ma, Q. Wen, P.H. Gao, Z. Yang, Y.C. Guo, J.P. Li, M.X. Liang: Int. J. Cast Met. Res. 31 (2018) 230. DOI:10.1080/13640461.2017.1409450

(Received November 15, 2018; accepted January 31, 2019; online since June 5, 2019)

Correspondence address

Zhijun Ma
School of Materials and Chemical Engineering
Xi'an Technological University
Xuefu Middle Road
Xi'an, 710021
P.R. China
Tel.: +86 029 8320 8080
Fax: +86 029 8320 8080
E-mail: 9216053@qq.com
Web: www.xatu.edu.cn

Bibliography
DOI 10.3139/146.111780
Int. J. Mater. Res. (formerly Z. Metallkd.)
110 (2019) 7; page 591 – 599

ISSN 1862-5282